Supplementary Information

Linking interfacial chemistry of CO_2 to surface structures of hydrated metal oxide nanoparticles: Hematite

I.V. Chernyshova, S. Ponnurangam, and P. Somasundaran*

A NSF I/UCRC Center for Particulate & Surfactant Systems (CPaSS), Columbia University, New York, 10027 NY

Table of content

Synthesis details

38 nm size hematite NPs were synthesized by forced hydrolysis.[1] Namely, 8.08 g of ferric nitrate was added into 1 L of 0.002 HCl heated to 98°C. This suspension was aged in the oven at 98°C for 7 d. After the synthesis, the suspension was cooled overnight and then was dialyzed against singly distilled water until the conductivity of the dialysis water reached that of the pure water, generally taking ten to fourteen days depending on the synthesis method. The synthesis details as well as the characterization of 7-nm hematite and ferrihydrite which were used for comparison are provided elsewhere.[2]

XRD (X-ray diffraction), BET (Brunauer, Emmet, and Teller) surface area, and surface charge characterization

The X-ray diffractogram was taken using a Scintag Model X2 X-ray powder diffractometer with a theta-theta geometry. The system includes a CuK_α (λ = 0.154 nm) radiation source operated at 45 kV and 35 mA and a Peltier cooled Si (Li) solid-state detector filtering CuK_β filtration radiation. The scan step size was 0.05 deg. The freeze-dried NPs were spun as an even layer on a microscope glass slide in

order to minimize the possibility of any preferential orientation of the NPs on the sample surface. Details of the Williamson–Hall analysis can be found elsewhere.[3]

Estimates of the surface area were made with a single-point BET N_2 adsorption isotherm obtained using a Monosorb (Quantachrome) surface area analyzer. The sample was degassed at 50°C for 180 minutes before measurements were taken. Two replicate measurements were performed, which agreed within less than 5%.

Zeta (ζ) potential was measured using a Zeta Sizer instrument, Nano-ZS at a solids loading of 0.005–0.01 vol% and a background electrolyte concentration of 0.01 M $NaNO_3$. Measurements were performed within a pH range of 4–10, and the pH of each subsample was adjusted using NaOH and/or HNO_3. The samples were equilibrated for one day at these pHs and were adjusted again for two hours before the actual measurement. The measurement was performed in duplicate. The isoelectric point (IEP) value of 9.3 was found from the dependence of zeta potential on pH (Figure S1).

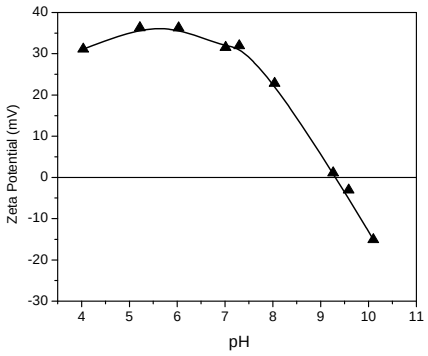

Figure S1. Zeta potential of hematite NPs

Point of zero charge (PZC) was measured using the pH drift method[4] in a glove box flushed with N_2 gas at room temperature. pH was measured using an Accumet combination double-junction Ag/AgCl reference pH electrode upon slow stirring of the suspensions. Only freshly de-carbonated triply-distilled water (TDW) was used, which was de-carbonated by boiling TDW several hours with N_2 bubbling. For pH adjustments, we used 0.01M solutions of either HNO_3 prepared in decarbonated TDW or NaOH prepared from a Dilut-It analytical NaOH (Baker). The NP suspension was decarbonated by N_2 bubbling for one day at least, divided into 4 portions 40 ml each and pH of each portion was adjusted using 0.01M NaOH. After stabilization of the suspension pH value (0.5–1 h), a weight of $NaNO_3$ was added to increase the suspension ionic strength to 0.1M. When the pH again stabilized, which usually took from 10 to 30 min, this value was measured and the change in pH, ΔpH, was determined by the difference (inclusive of

sign) between the final pH and the initial pH. At the zero point of charge, ΔpH = 0. The measurement was performed in duplicate. These measurements gave PZC of 9.2.

X-ray photoelectron spectroscopy (XPS) analysis

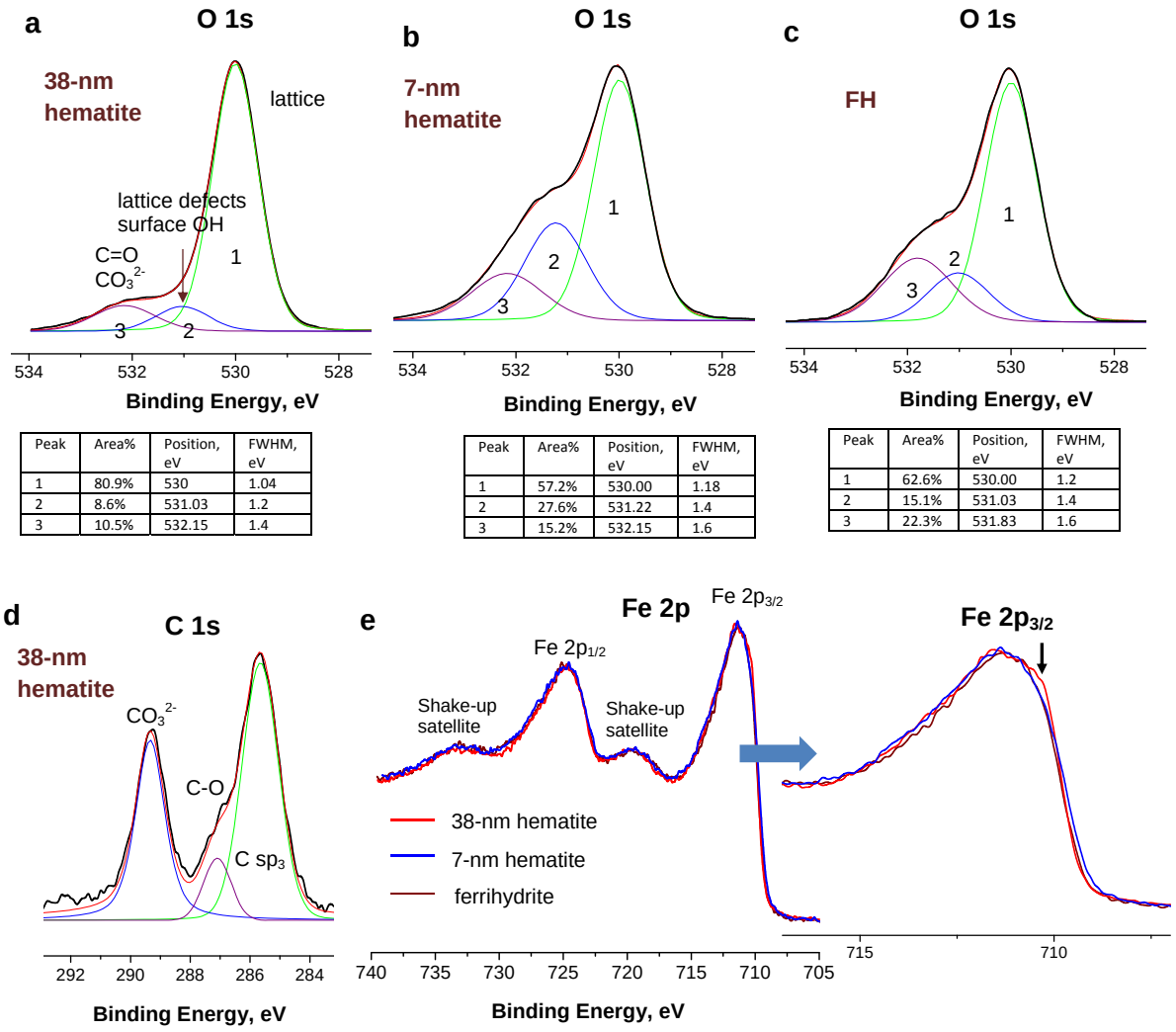

Peak	Area%	Position, eV	FWHM, eV
1	80.9%	530	1.04
2	8.6%	531.03	1.2
3	10.5%	532.15	1.4

Peak	Area%	Position, eV	FWHM, eV
1	57.2%	530.00	1.18
2	27.6%	531.22	1.4
3	15.2%	532.15	1.6

Peak	Area%	Position, eV	FWHM, eV
1	62.6%	530.00	1.2
2	15.1%	531.03	1.4
3	22.3%	531.83	1.6

Figure S2. (a–c) XPS core-level O 1s (with the curve fitting results) of (**a**) 38-nm hematite, (**b**) 7-nm hematite, and (**c**) FH; (**d**) C 1s of 38-nm hematite; and (**e**) Fe 2p spectra of hematite and ferrihydrite (FH) NPs. Arrow in the expanded Fe $2p_{3/2}$ peak shows the ligand-field multiplet-splitting shoulder in the spectrum of 38-nm hematite.

XPS spectra were collected with a Perkin Elmer PHI 5500 instrument using monochromatic AlKα X-rays with pass energies of 17.6 eV at resolution of 0.9 eV at take-off angle of mm45° at pressures of less than 1×10^{-8} Torr, calibrated using the Au($4f_{7/2}$) peak at 84.0 eV. Regional scans within from 10 to

50 eV windows widths were collected at 0.1 eV steps. To curve fit the O 1s spectra, the Shirley function[5] was used to subtract the background. The deconvolution kernel was a Gaussian-Lorentzian (10%) function. The peak position calibrated by assuming a common Binding energy (BE) for the O 1*s* core-level electrons of lattice oxygen.[6-8] The XPS spectra were reproduced on 3 samples in terms of peak widths, shapes, and positions, as well as surface atomic concentrations, within the experimental error of the method.

Figure S2 shows the O 1s, Fe 2p, and C1s regions for these NPs. For comparison are shown the O1s and Fe 2p core-level photoemissions for 7-nm hematite and ferrihydrite (FH) which were used in our previous studies.[2, 7, 9, 10] The Fe 2p spectra of all the NPs (Figure S2e) are typical of ferric cations.[11, 12] As compared to 7-nm hematite and FH, 38-nm hematite is characterized by a slightly more pronounced multiplet shoulder at the low binding energy side of the Fe $2p_{3/2}$ peak (marked by an arrow). This feature indicates that, among the NPs, 38-nm hematite are most crystalline[13] which results in its higher Fe–O covalency[2] (associated with a higher electron density on ferric cations).

The O 1s spectra of the NPs (Figure S2a) contain, apart from the principal peak of lattice O^{2-} at 530.0 eV (peak 1), two additional peaks shifted to higher binding energies by ~1 and 2 eV (peaks 2 and 3, respectively). Peak 2 is due to lattice oxygen in a defective oxide environment[14] and/or surface hydroxyls.[15, 16] Peak 3 (shifted by ~2 eV) can be assigned to oxygen-containing carbon species (C–O and O=C–O) including carbonate.[16-18] It is worth noting that all the O 1s spectra do not exhibit the peak of physisorbed water which is commonly shifted by ~3 eV relative to the main oxide peak 1,[16] meaning that the NPs are dehydrated under the UHV conditions. Importantly, as compared to 7-nm hematite and ferrihydrite, 38-nm hematite is characterized by the lowest intensity ratio of peak 2 to peak 1, suggesting the lowest surface concentration of hydroxyls, and hence the lowest ability of these NPs to polarize and dissociate chemisorbed water.

Finally, the C 1 s spectrum of 38-nm hematite (Figure S2d) contains peaks at 284.9 and 286.34 eV of the sp^3 and C–O carbon, respectively, as well as a peak at 288.6 eV. The latter can be assigned to adsorbed carbonate based on its narrower width as compared to the 284.9-eV peak of the sp^3 carbon. The carbonate peak gives the C/Fe atomic ratio of 0.10±0.01 for the surface coverage of carbonate under UHV conditions. When compared to the C/12Fe atomic ratio of 0.42±0.2 for a well-packed self-assembled monolayer of dodecanoate (C12) on hematite (Ref.[19]), this surface coverage of carbonate corresponds to about 0.2 monolayer.

Raman spectroscopy

Raman spectra were measured on a wet paste of the NPs using a Labram ARAMIS confocal Raman microscope. A 17-mW 633-nm HeNe laser was used as the excitation source, and the beam power was attenuated by a D2 filter to reduce heating of the sample by the laser beam.

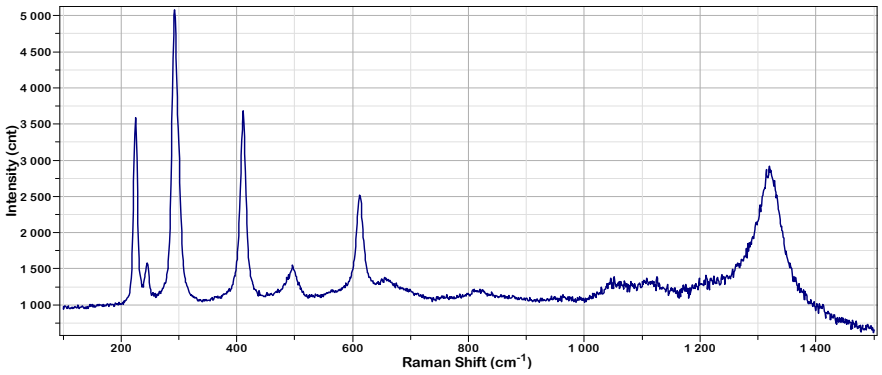

Figure S3. Raman spectrum of wet H38 NPs

Additional FTIR data

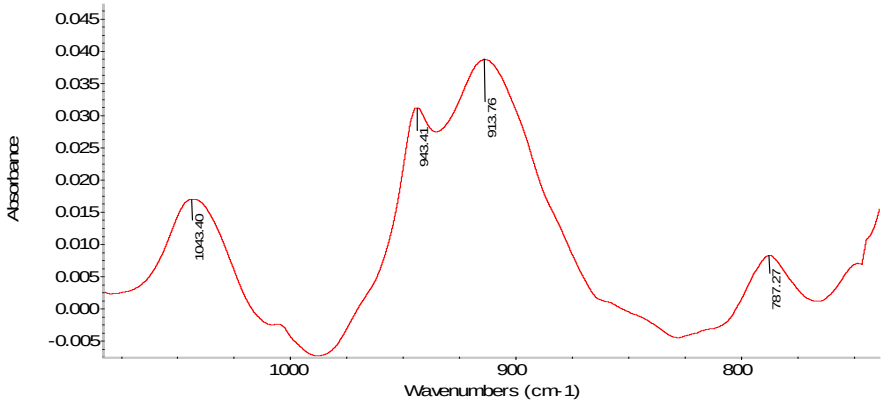

Figure S4. The region of multiphoton modes in the *in situ* FTIR spectrum of 38-nm hematite in D_2O at pH 3.0 shown in Figure 6a. There is no effect of H/D exchange on bands at 787, 914, and 943 cm-1, in agreement with their assignment.

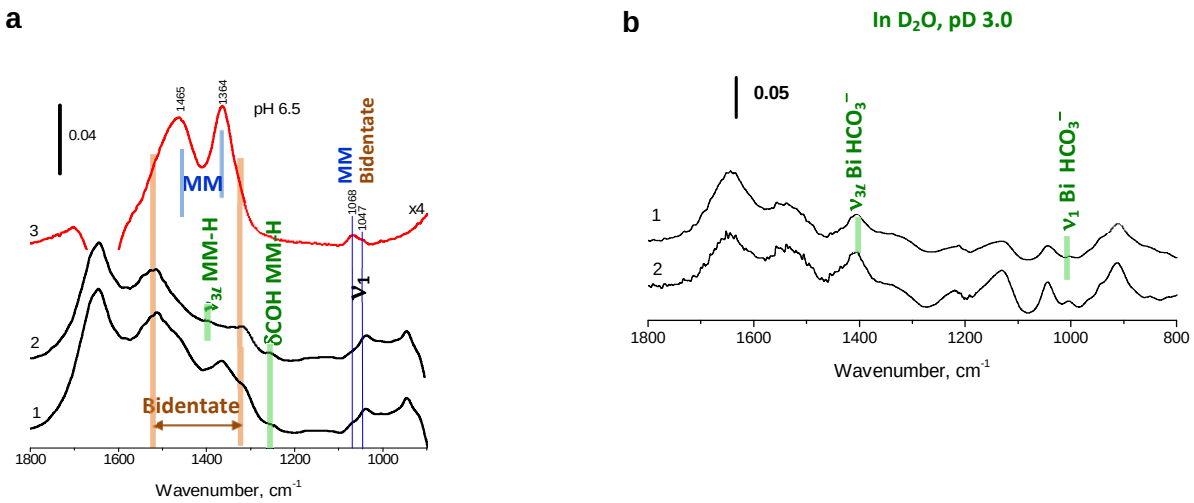

Figure S5. Effect of ionic strength (0.1M NaCl) on in situ FTIR-HATR spectra of 38nm hematite NPs at (a) in H_2O at pH 6.5: 1 — no ionic strength adjustment, 2 — 0.18 M NaCl, 3 — difference spectrum (multiplied by 4) and (b) at pD=3.0 in D_2O. 1—no NaCl; 2—0.1M NaCl. MM=mononuclear monodentate carbonate, MM-H=mononuclear monodentate bicarbonate. Bi -HCO_3^- = bidentate bicarbonate.

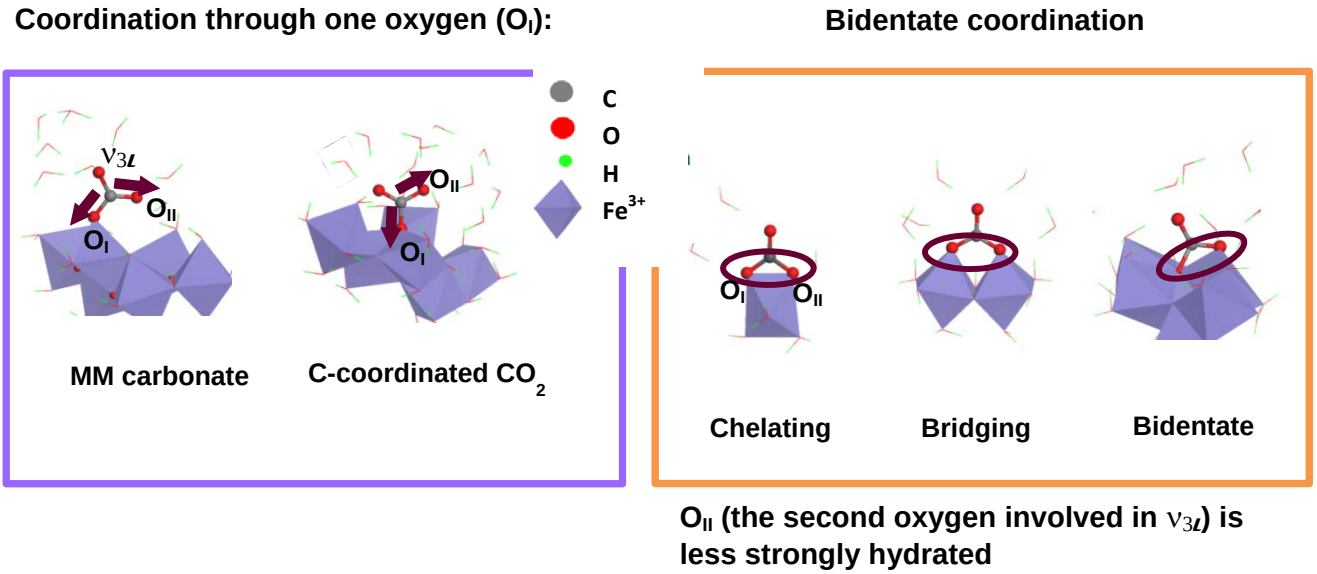

Figure S6. Different hydration of oxygen atoms O_{II} in carbonate/CO_2 species in left and right panels. O_{II} is H-bonded to water molecules in monodentate complexes (left panel) and is coordinated to surface Fe^{3+} in bidentate complexes (right panel). Left panel also shows the vibration form of the ν_{3t} mode of

adsorbed carbonate. This mode involves mainly in-phase stretching vibrations of the C–O_I and C–O_{II} bonds, where O_I is coordinated to surface Fe^{3+}.

Location of *δCOH bands of bidentate bicarbonate*

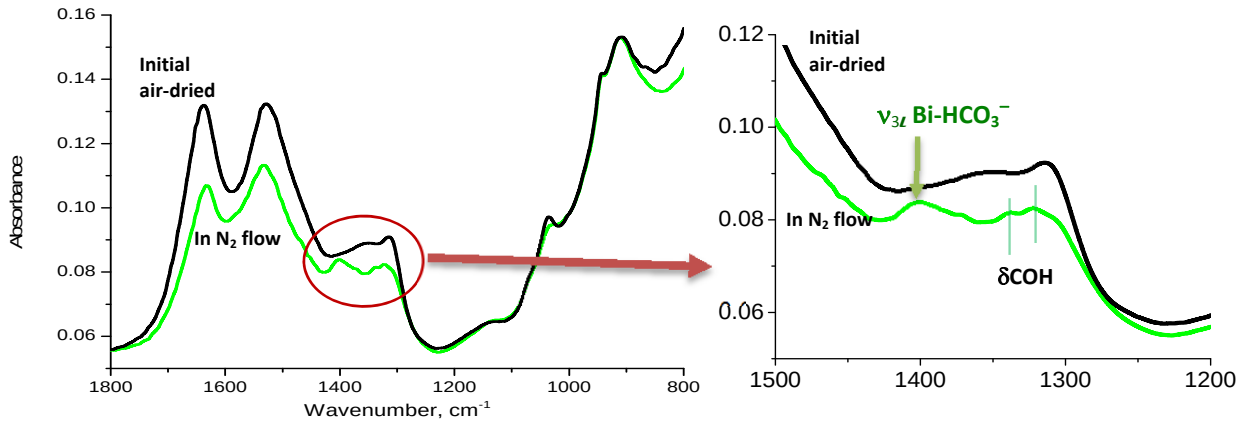

Figure S7. HATR spectra of 38-nm hematite NPs (black) air-dried at 40% relative humidity and (green) in a N_2 flow for 10 min. Bi-HCO3 stands for bidentate bicarbonate.

To locate the δCOH bands of bidentate bicarbonate, we study the evolution of the FTIR spectrum of the air-dried NPs in the N_2 flow. As seen from Figure S7, the initial NPs exposed to air at a relative humidity of 40% are mostly covered by bidentate carbonate (1316 and 1528 cm^{-1}) and MM carbonate (1353 and 1470 cm^{-1}). The bands of the corresponding bicarbonates, if any, are masked by the strong bands of the carbonates. We *a priori* expect that the weaker complexes (MM carbonate and MM bicarbonate) will more easily be desorbed by exposure to the N_2 atmosphere, leaving behind bidentate carbonate which tends to be protonated.[20-22] Therefore, under these conditions, the masking bands of MM carbonate and MM bicarbonate are removed and the protonation equilibrium at the surface shifts from bidentate carbonate to its protonated form. In accordance, in the N_2 atmosphere, the MM carbonate bands decrease in intensity. Instead, a broad band at 1410 cm^{-1} and new narrow bands at 1338 and 1320 cm^{-1} appear. The 1410-cm^{-1} is assignable to the ν_{3l} mode of bidentate bicarbonate, while the bands at 1338 and 1320 cm^{-1} to be the δCOH modes.

Curve fitting of difference spectra shown in Figure 4b of the main text

Baseline:Spline

Chi^2=3.74116E-008 Adj. R-Square=9.99222E-001 # of Data Points=682.

SS=2.48039E-005 Degree of Freedom=663.

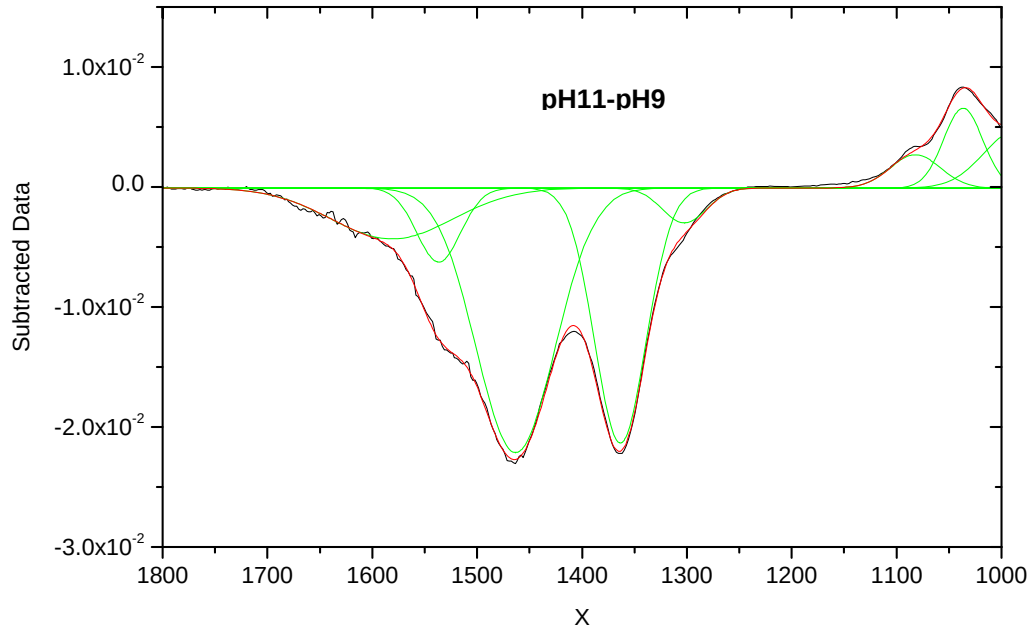

Fitting Results

Peak Index	Peak Type	Area Intg	FWHM	Max Height	Center Grvty	Area IntgP
1.	Gaussian	0.36175	72.91258	0.00473	986.05134	6.81257
2.	Gaussian	0.16622	56.29097	0.00277	1082	3.13032
3.	Gaussian	-1.30046	57.48885	-0.02125	1363.2927	-24.49079
4.	Gaussian	-0.32347	49.267	-0.00617	1536.6	-6.09168
5.	Gaussian	-2.07348	88.33138	-0.02205	1463.30855	-39.04862
6.	Gaussian	-0.61909	137.03292	-0.00424	1581.14752	-11.659
7.	Gaussian	-0.15345	49.461	-0.00291	1302.3	-2.88986
8.	Gaussian	0.31208	44.14391	0.00664	1036.52442	5.87716

Figure S8 (continued)

Baseline:Spline

Chi^2=1.58373E-008 Adj. R-Square=9.99799E-001 # of Data Points=312.

SS=4.60865E-006 Degree of Freedom=291.

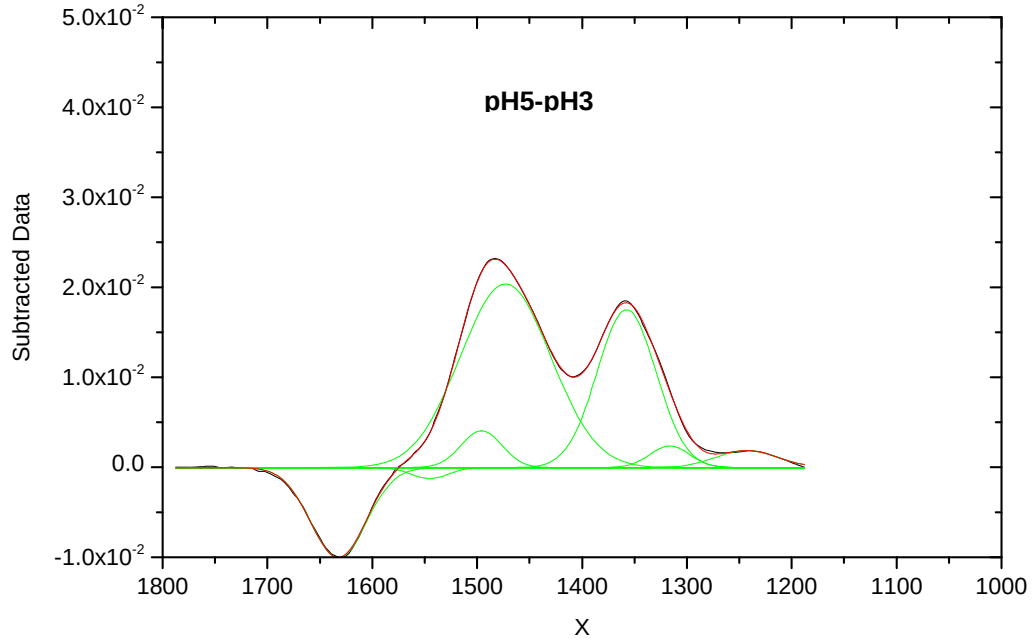

Fitting Results

Peak Index	Peak Type	Area Intg	FWHM	Max Height	Center Grvty	Area IntgP
1.	Gaussian	1.2358	66.184	0.01754	1357.5	27.76365
2.	Gaussian	0.20147	46.17	0.0041	1495.8	4.52625
3.	Gaussian	-0.66495	62.43274	-0.01001	1632.16699	-14.93881
4.	Gaussian	0.1363	69.27855	0.00191	1242.92892	3.06203
5.	Gaussian	0.11579	45.04375	0.00241	1316.18928	2.60136
6.	Gaussian	2.20494	101.45473	0.02042	1472.91299	49.53659
7.	Gaussian	-0.05267	40.90458	-0.00121	1545.21157	-1.18328
8.	Gaussian	0	0.00426	202.15578	1580.52916	0
9.	Gaussian	0	0	0	1242.92892	0

Figure S8. Curve fitting of two difference spectra shown in Figure 4b performed using Origin Pro 8.5.1.

TEM of annealed 38-nm hematite

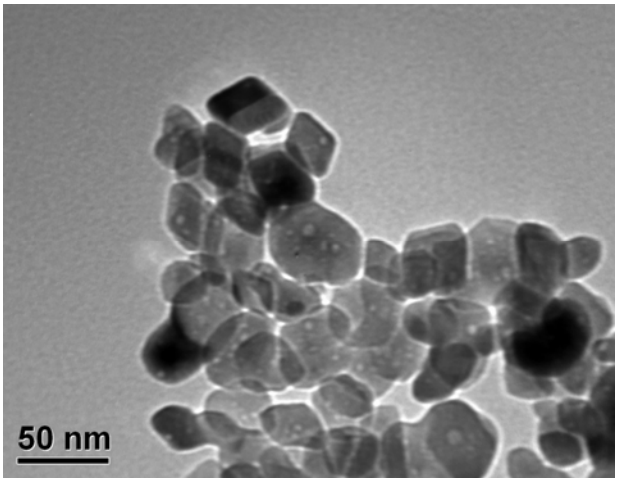

Figure S9. TEM image of 38-nm hematite after annealing at 673K in N_2 flow for 3 h. FTIR spectra of these NPs after annealing and subsequent rehydration are shown in Figures 6 and 8a, respectively.

Surface recognition of bidentate carbonate

To study the geometrical compatibility of the bidentate carbonate with the atomic arrangements on different hematite surfaces, we analyzed several non-hydrated stoichiometric terminations created from the experimental crystallographic structure of hematite using Material Studio™ (Accelrys Inc., San Diego, CA, USA). We selected hexagonal [(110) and (100)], rhombohedral [(101) and (012)], as well as iron-depleted pinacoid (001) surfaces because they are most common for hematite NP synthesized by forced hydrolysis.[23] Although the real hydrated stoichiometric terminations structurally differ from the ideal cleavages due to the atomic relaxations, they preserve the main topology of the ideal counterparts,[24] because chemisorbed water saturates the bonds created by the surface cleavage and hence decreases the surface energy.

As seen from Figure S9, in the case of (110), (100), and iron-depleted (001), the μ_3-O site is sterically blocked as it is buried inside the surface (below the plane drawn through the topmost cations). This site is inert with respect to the nucleophilic attack on CO_2. Although this site protrudes out of the Fe-Fe plane in the case of the rhombohedral (101) and (012) facets, the angle between the dangling bond of 5-coordinated Fe and the Fe–O bond connecting this Fe to the μ_3-O^- site is too large (85.8 and 102.7°, respectively) as compared to the internal O–Fe–O angle of bidentate CO_2 of 67±2°. It follows that the formation of the bidentate carbonate complex on the (101) and (012) surfaces requires significant reconstruction of these surfaces

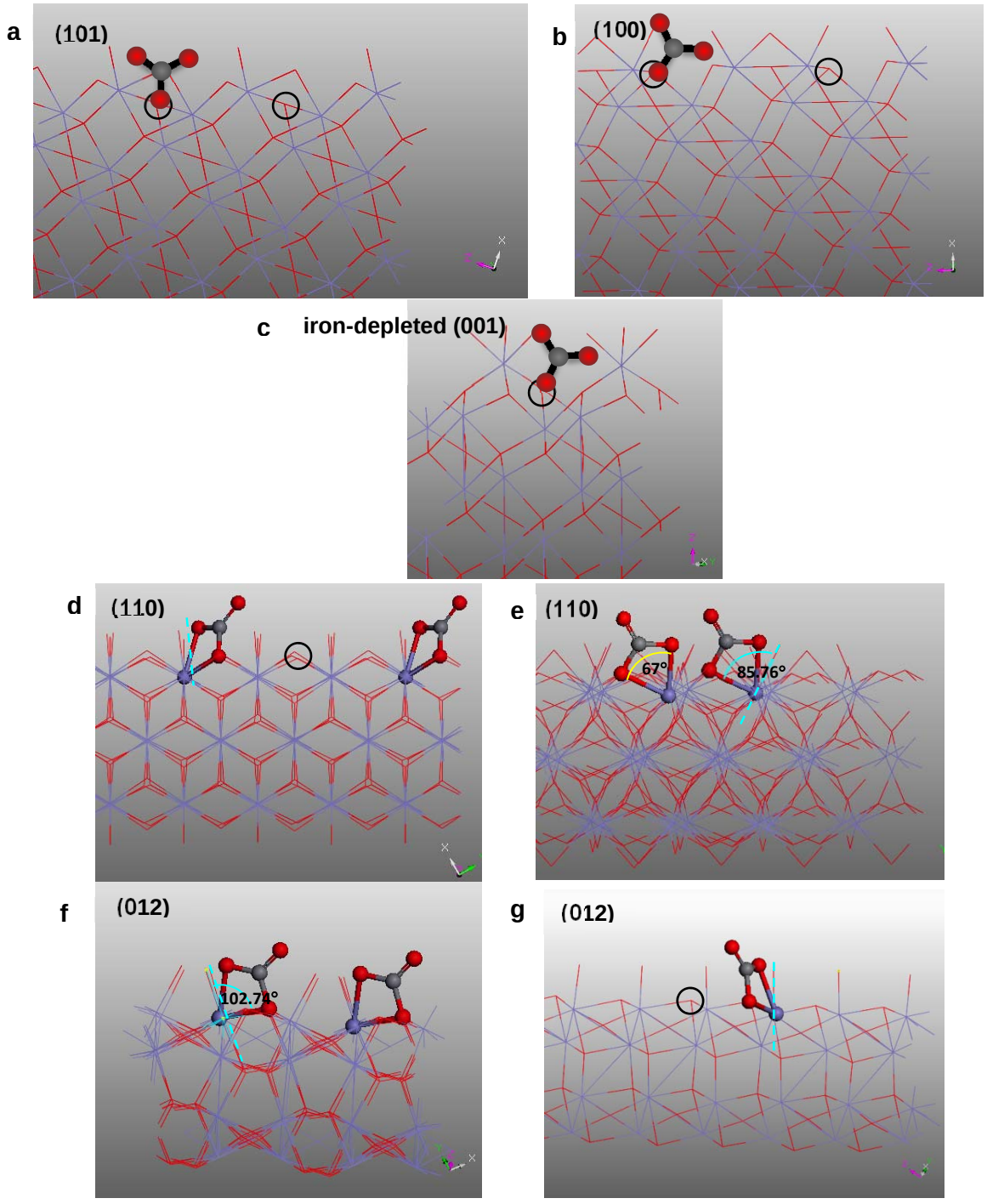

Figure S10. Steric constrains on the accommodation of the bidentate carbonate complex by (**a**) (101), (**b**) (100), (**c**) iron depleted (001), (**d,e**) (110), (**f,g**) (012) hematite surfaces. The surfaces are shown oxygen-terminated and unrelaxed. Circles show μ_3-O^- adsorption sites, dashed cyan line shows the direction of the dangling bond of 5-coordinated ferric cation that hosts an imaginary bidentate carbonate complex attached to the μ_3-O^- adsorption sites on (110) and (012) surfaces. The internal O–Fe–O angle of bidentate CO_2 is 67±2° (yellow line). Atom codes: red-O, grey-C, blue-Fe

References

1. R. M. Cornell and U. Schwertmann, *The Iron Oxide: Structure, Properties, Reactions and Uses*, VCH, Weinheim, 1996.
2. I. V. Chernyshova, S. Ponnurangam and P. Somasundaran, *Physical Chemistry Chemical Physics*, 2010, **12**, 14045-14056.
3. I. V. Chernyshova, M. F. Hochella and A. S. Madden, *Physical Chemistry Chemical Physics*, 2007, **9**, 1736-1750.
4. A. L. Mular and R. B. Roberts, *Canadian Mining and Metallurgical Bulletin*, 1966, **59**, 1329-&.
5. D. A. Shirley, *Physical Review B*, 1972, **5**, 4709-&.
6. T. Yamashita and P. Hayes, *Applied Surface Science*, 2008, **254**, 2441-2449.
7. I. V. Chernyshova, S. Ponnurangam and P. Somasundaran, *J. Catalysis*, 2011, **282** 25–34.
8. K. Shimizu, A. Shchukarev, P. A. Kozin and J. F. Boily, *Surface Science*, 2012, **606**, 1005-1009.
9. S. Ponnurangam, I. V. Chernyshova and P. Somasundaran, *Journal of Physical Chemistry C*, 2010, **114**, 16517–16524.
10. M. Villalobos and J. O. Leckie, *Geochim. Cosmochim. Acta*, 2000, **64**, 3787-3802.
11. N. S. McIntyre and D. G. Zetaruk, *Analytical Chemistry*, 1977, **49**, 1521-1529.
12. A. T. Kozakov, K. A. Guglev, V. V. Ilyasov, I. V. Ershov, A. V. Nikol'skii, V. G. Smotrakov and V. V. Eremkin, *Phys. Solid State*, 2011, **53**, 41-47.
13. T. Droubay and S. A. Chambers, *Physical Review B*, 2001, **64**.
14. C. Chen, S. J. Splinter, T. Do and N. S. McIntyre, *Surface Science*, 1997, **382**, L652-L657.
15. X. Y. Deng, J. Lee, C. J. Wang, C. Matranga, F. Aksoy and Z. Liu, *Journal of Physical Chemistry C*, 2010, **114**, 22619-22623.
16. S. Yamamoto, T. Kendelewicz, J. T. Newberg, G. Ketteler, D. E. Starr, E. R. Mysak, K. J. Andersson, H. Ogasawara, H. Bluhm, M. Salmeron, G. E. Brown and A. Nilsson, *Journal of Physical Chemistry C*, 2010, **114**, 2256-2266.
17. G. Beamson and D. Briggs, *High Resolution XPS of Organic Polymers. The Scienta ESCA 300 Database*, Wiley, Chichester, 1992.
18. J. K. Heuer and J. F. Stubbins, *Corrosion Science*, 1999, **41**, 1231-1243.
19. I. V. Chernyshova, S. Ponnurangam and P. Somasundaran, *Langmuir*, 2011, **27**, 10007-10018.
20. L. Ferretto and A. Glisenti, *Journal of Molecular Catalysis a-Chemical*, 2002, **187**, 119-128.
21. M. Casarin, D. Falcomer, A. Glisenti and A. Vittadini, *Inorg. Chem.*, 2003, **42**, 436-445.
22. C. Morterra and G. Magnacca, *Catalysis Today*, 1996, **27**, 497-532.
23. N. J. Reeves and S. Mann, *Journal of the Chemical Society-Faraday Transactions*, 1991, **87**, 3875-3880.
24. K. S. Tanwar, C. S. Lo, P. J. Eng, J. G. Catalano, D. A. Walko, G. E. Brown, G. A. Waychunas, A. M. Chaka and T. P. Trainor, *Surface Science*, 2007, **601**, 460-474.